

See discussions, stats, and author profiles for this publication at: <https://www.researchgate.net/publication/231648364>

Methane Hydrate Nucleation Rates from Molecular Dynamics Simulations: Effects of Aqueous Methane Concentration, Interfacial Curvature, and System Size

ARTICLE *in* THE JOURNAL OF PHYSICAL CHEMISTRY C · OCTOBER 2011

Impact Factor: 4.77 · DOI: 10.1021/jp206483q

CITATIONS

47

READS

67

6 AUTHORS, INCLUDING:



Gregg T. Beckham

National Renewable Energy Laboratory

90 PUBLICATIONS 2,115 CITATIONS

[SEE PROFILE](#)



Carolyn Ann Koh

Colorado School of Mines

197 PUBLICATIONS 5,083 CITATIONS

[SEE PROFILE](#)



David Wu

Colorado School of Mines

98 PUBLICATIONS 1,629 CITATIONS

[SEE PROFILE](#)

Methane Hydrate Nucleation Rates from Molecular Dynamics Simulations: Effects of Aqueous Methane Concentration, Interfacial Curvature, and System Size

Matthew R. Walsh,[†] Gregg T. Beckham,^{†,‡} Carolyn A. Koh,[†] E. Dendy Sloan,[†] David T. Wu,^{†,§} and Amadeu K. Sum^{*,†}

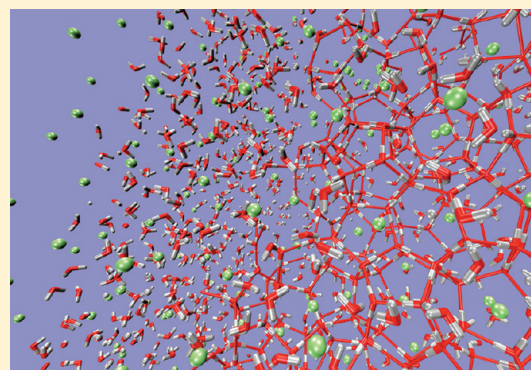
[†]Center for Hydrate Research, Chemical & Biological Engineering Department, Colorado School of Mines, Golden, Colorado 80401, United States

[‡]National Bioenergy Center, National Renewable Energy Laboratory, Golden, Colorado 80401, United States

[§]Department of Chemistry, Colorado School of Mines, Golden, Colorado 80401, United States

 Supporting Information

ABSTRACT: Methane hydrate nucleation rates are reported from over 200 μ s of molecular dynamics simulations across a range of thermodynamic conditions and varying degrees of methane–water interfacial curvature. Calculated nucleation rates increase with aqueous phase methane concentration (X_{CH_4}), consistent with experimental results. The effect of interfacial curvature on X_{CH_4} is quantified, with dissolved methane concentration increasing with the degree of curvature (i.e., the number of dimensions in which curvature exists). Nucleation rates are reported for system sizes of 3456 and 13 824 molecules ($\text{H}_2\text{O} + \text{CH}_4$). Among the smaller simulation systems (which comprise the majority of the data), the calculated hydrate nucleation rates follow the same trend when plotted against X_{CH_4} regardless of whether the predominant contribution to the effective system pressure is the simulation barostat or the methane–water interfacial curvature (Young–Laplace pressure). The incipient hydrate nuclei are destabilized in the immediate vicinity ($\sim 1 \text{ nm}$) of the methane–water interface, and the calculated nucleation rates for the larger simulation systems (in which the incipient hydrate solids are less affected by interfacial destabilization) fall above the trend observed in the smaller systems.



1. INTRODUCTION

Clathrate hydrates are ice-like inclusion compounds that form when small guest molecules such as methane, nitrogen, carbon dioxide, and hydrogen are trapped (enclathrated) inside hydrogen-bonded water cages in a crystal lattice.¹ The formation of clathrate hydrates of natural gases (also called gas hydrates) is a major impediment to operational safety and economic viability in hydrocarbon production; preventing, mitigating and remediating the formation of gas hydrates in pipelines are among the costliest tasks in the growing field of flow assurance engineering,^{1,2} and gas hydrate formation can disrupt seafloor oil-spill mitigation efforts, as during the 2010 Macondo-252 spill.³ Gas hydrates are abundant geologically where the pressure, temperature, and chemical conditions are appropriate and have gained attention as a potential source of energy.⁴ The production of natural gas from hydrates will likely require the processing of larger volumes of produced water relative to conventional operations, making hydrate inhibition and reformation—prevention strategies relevant to project viability.⁵ An understanding of the controlling variables of hydrate formation will allow for safer and more efficient energy production and delivery and could improve the

economics of some of the more exotic gas hydrate applications such as separation,⁶ refrigeration,⁷ and gas-storage processes.^{2,8,9} Experimental and complementary theoretical studies have explored both induction phenomena^{10–17} and the mechanisms^{18–31} of hydrate nucleation. Molecular simulation studies have focused primarily on the mechanisms of clathrate hydrate nucleation,^{32–45} adding nanoscale insights to the evolving state of the art in hydrate formation kinetics. Here, from over 150 independent, microsecond-scale molecular dynamics (MD) simulations, we investigate hydrate nucleation induction phenomena over a range of thermodynamic conditions and varying degrees of interfacial curvature. First we discuss the effects of interfacial curvature, temperature, and simulation barostat pressure on aqueous phase methane concentration (X_{CH_4}). We then report the observed nucleation induction times at each set of conditions, showing a decrease in induction times (and a decrease in their stochasticity) at higher aqueous phase methane concentrations.

Received: July 8, 2011

Revised: September 21, 2011

Published: September 22, 2011

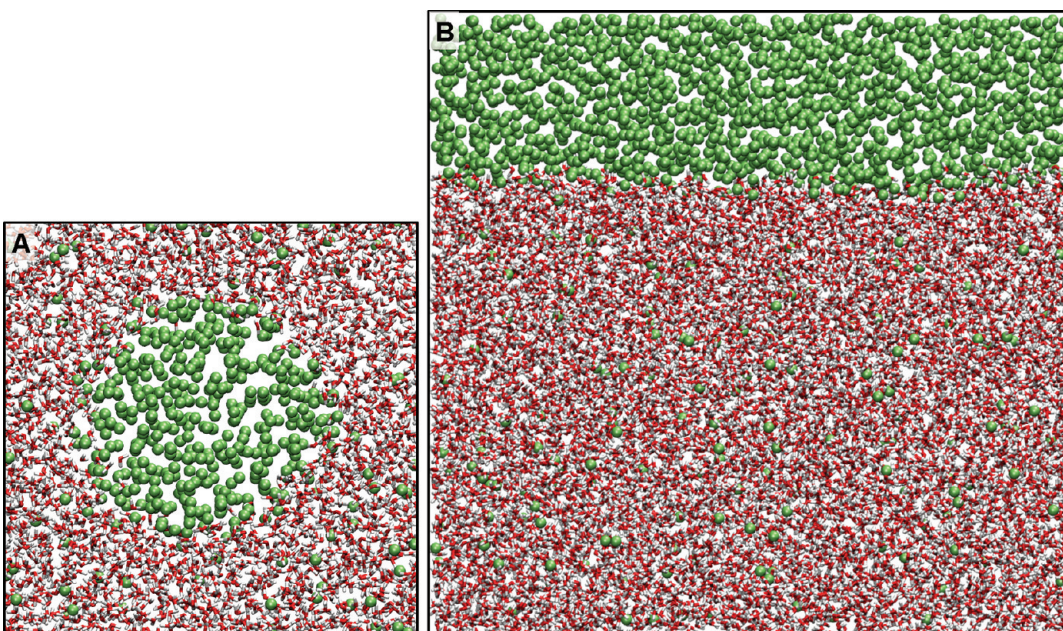


Figure 1. Different system sizes and curvatures implemented in this study. (A) Systems with interfacial curvature (cylindrical curvature shown here as an example) contain 3456 molecules and the cubic simulation systems are ~ 5 nm per edge. (B) Systems with flat interfaces contain 13 824 molecules and the cubic simulation systems are ~ 8 nm per edge. Methane molecules shown as green spheres and water molecules shown in red (oxygen) and white (hydrogen).

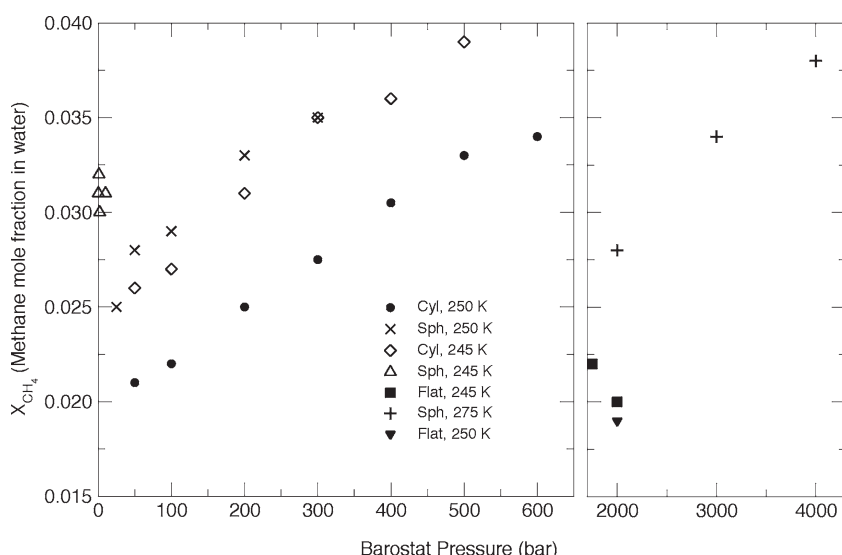


Figure 2. Prenucleation methane mole fraction in the aqueous phase for the NPT simulations performed in this study, calculated at the thermodynamic conditions investigated in the study, and at the different interfacial curvatures implemented.

Finally, we report hydrate nucleation rates calculated at all conditions studied and discuss how these calculations are subject to multiphase simulation system size effects.

2. METHODS AND MODELS

To calculate the nucleation rate at a given set of conditions (pressure, temperature, and interfacial geometry), multiple, independent microsecond-scale MD simulations (six simulations of $1.8 \mu\text{s}$ each in most cases) were performed at the conditions of interest. The first two columns of Table S1 in Supporting

Information list the conditions at which all simulations were performed. Each simulation was monitored for nucleation, the time to nucleation (induction time) was recorded for each reactive (nucleating) trajectory, the total simulation time was recorded for each nonreactive trajectory, and the nucleation rate was calculated using⁴⁶

$$\text{rate} = \frac{N_R}{\left(\sum_{i=1}^{N_R} \tau_i + \sum_{j=1}^{N_{NR}} \tau_j \right) \cdot V_{\text{liq}}} \quad (1)$$

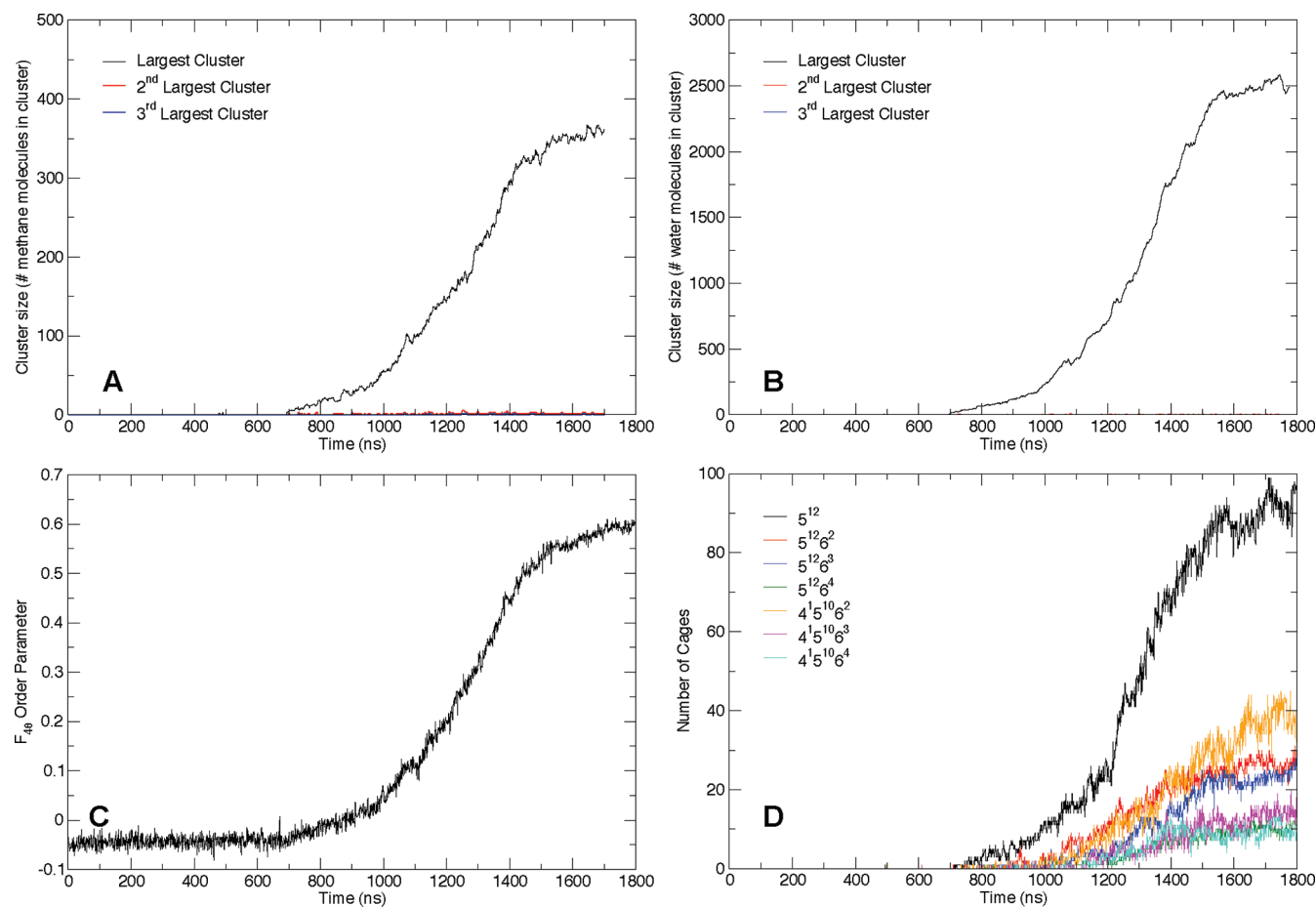


Figure 3. Order parameters used to calculate induction times to nucleation for an example trajectory (250 K, 100 bar, spherical interfacial curvature, induction time = 700 ns). (A) Methane and (B) water solid-like clustering. Solid-like bonds are defined as existing between two molecules within 0.8 nm (for CH₄) or 0.3 nm (for H₂O) of each other, uninterrupted for 25 ns. We investigated induction times, prenucleation clustering attempts, and growth with a variety of bond-pair time cutoffs in the clustering algorithm. When compared with the results obtained using a cutoff of 25 ns (which we used to reduce noise), the same induction times and postnucleation number of solid clusters were observed at cutoff values lower than 25 ns, though the prenucleation noise increased as the cutoff was decreased. (C) F₄ order parameter and (D) dominant cage-type evolutions for verification of induction times.

where N_R is the number of reactive (nucleating) trajectories, N_{NR} is the number of nonreactive trajectories, τ_i is the induction time for the i th reactive trajectory, τ_j is the total simulation time for the j th nonreactive trajectory, and V_{liq} is the volume of the aqueous phase.

Simulations were initiated from fully disordered two-phase mixtures of methane and water, with three different types of methane–water interfacial geometry (spherical, cylindrical, and slab geometry). Interfacial curvature increases the concentration of gas molecules dissolved in the aqueous phase,^{39,47} giving an extra degree of freedom (along with pressure and temperature) with which to manipulate the prenucleation fluid mixture conditions. The systems with spherical or cylindrical interfacial curvature consisted of 2944 water and 512 methane molecules, while systems with slab geometry consisted of 11 776 water and 2048 methane molecules. The larger simulation size for the systems with slab geometry prevented the spontaneous formation of a spherical or cylindrical nanobubble (i.e., the type of event seen at ~ 200 ns in Figure 1 of Walsh et al.³⁹). The preparation of initial configurations differed depending on the desired interfacial geometry (spherical, cylindrical, or flat). To generate curved (spherical or cylindrical) interfaces, 64 unit cells of sI

hydrate were partially melted at 425 K and 100 bar for 4 ns, followed by complete melting at 305 K and 100 bar for 15 ns; this yielded a system with a spherical gas phase. A configuration with a cylindrical gas phase was created by performing NVT simulations at 550 K for 8 ns initiated from the configuration with a spherical gas phase, allowing the spherical bubble to expand across one dimension of the simulation box to create a cylindrical bubble. To generate configurations with a flat interface (slab phases), 256 unit cells of sI hydrate were melted with an anisotropic barostat (with two fixed dimensions) at 425 K and 100 bar, yielding a vapor–liquid mixture with the interface perpendicular to the mobile dimension; the resulting simulation box oscillated in the mobile direction, and configurations were chosen for subsequent quenching at points along the trajectory when the simulation box happened to be cubic. The cubic simulation boxes were ~ 5 nm per side in the smaller systems (3456 molecules) and ~ 8 nm per side in the larger systems (13 824 molecules) after quenching. Example configurations for the different system sizes and geometries are shown in Figure 1.

MD simulations were performed using Gromacs,⁴⁸ with the leapfrog algorithm used to integrate the equations of motion. Simulations were performed at hydrate-forming conditions^{49,50}

in the NPT or (density-equilibrated) NVT ensembles, and full periodic boundary conditions were applied in all directions. Pressure was controlled in *NPT* simulations with an isotropic Parrinello–Rahman barostat⁵¹ with a time constant of 4 ps, while temperature was controlled in all simulations with a Nosé–Hoover thermostat⁵² with a time constant of 2 ps. The TIP4P/Ice water model⁵³ and a united atom Lennard-Jones methane model⁵⁴ were implemented with Lorentz–Berthelot combining rules for methane–water interactions. The SETTLE algorithm⁵⁵ was used to maintain a rigid water geometry. A time step of 2 fs was used, with short-range interactions truncated at 1 nm. Long-range electrostatics corrections were computed with the smooth particle mesh Ewald summation algorithm with a Fourier spacing of 0.12 nm.⁵⁶

3. RESULTS AND DISCUSSION

3.1. Aqueous Phase Methane Concentration. Figure 2 shows the prenucleation aqueous methane mole fraction for the pressures, temperatures, and interfacial geometries studied. Figure S1, Supporting Information, describes the methods used to calculate the methane concentration in the aqueous phase. The third column of Table S1, Supporting Information, also lists the observed values of methane concentration. As expected, X_{CH_4} increases with increasing pressure, decreasing temperature, and increasing degree of interfacial curvature (slab < cylindrical < spherical). The increase in X_{CH_4} with increasing curvature is due to the effective pressure increase in the methane phase as governed by the Young–Laplace equation,⁴⁷ and previous MD simulations suggest that this relationship is valid even at the nanoscale.⁵⁷ The values of X_{CH_4} for the systems with flat interfaces illustrate the dramatic effect of having any interfacial curvature; in order to achieve comparable concentrations of methane in water at similar temperatures (245–250 K), it is necessary to set the barostat pressure at least an order of magnitude higher compared with systems with curved interfaces.

It is clear that interfacial geometry has an important effect on X_{CH_4} and should be considered when performing multiphase simulations. Recently, two groups used three-phase MD simulations to calculate several points along the liquid/hydrate/vapor equilibrium curve via the direct-coexistence method.^{50,58} While Conde et al. report direct-coexistence results using a flat vapor–liquid interface, Jacobson et al. implemented an interface with cylindrical curvature.⁵⁸ Given the results we report here, we expect the presence of interfacial curvature in direct coexistence studies to alter the calculated hydrate stability conditions by increasing the concentration of methane in the aqueous phase. It should be noted that despite their curved interface, Jacobson et al. report a negligible change in aqueous phase methane concentration compared with simulations with slab geometry.⁵⁸

3.2. Hydrate Nucleation Induction Times. For each reactive trajectory, the induction time was identified as the point at which the size of the largest solid-like cluster permanently deviated from zero (disregarding that the slope approached zero later in the simulation after solid hydrate had filled the box). Cluster analysis shows that in almost all cases, only one solid-like cluster nucleates and grows, though several exceptions are observed (an example of multiple hydrate nuclei is shown in Figure S2, Supporting Information). The induction times were verified with the evolution of the global F_4^{35} order parameter as well as the number of each of the seven most abundant cages to appear in our trajectories.⁵⁹ Figure 3 shows the evolution of these order

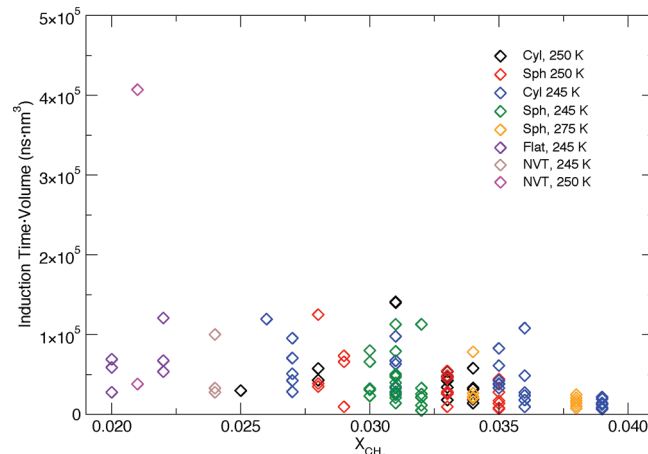


Figure 4. Induction times (multiplied by liquid volume) of all reactive trajectories obtained, with the conditions color-coded for ease of visualization (there is considerable overlap). Nonreactive simulations (which could be included as lower bounds for induction times) are not shown for clarity, but from Table S1, Supporting Information, it is clear that there are far more nonreactive trajectories at the lower concentrations (consistent with longer induction times and more data scatter while moving from right to left in the figure). These induction times (corrected for 50 ns of equilibration) were used in eq 1 for calculation of nucleation rates.

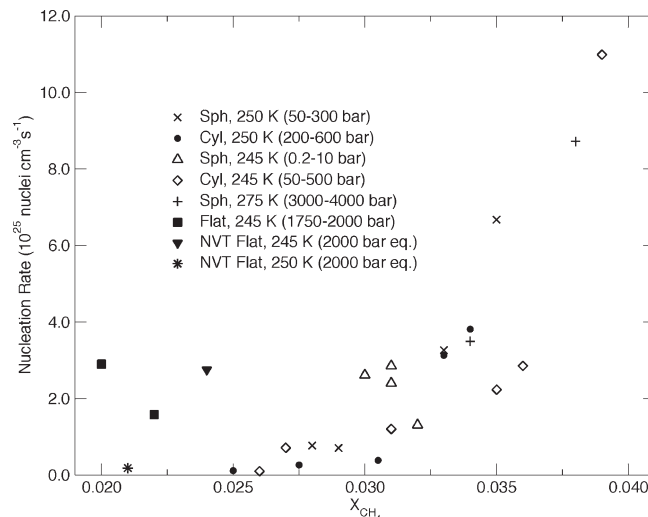


Figure 5. Hydrate nucleation rates calculated from the induction data shown in Figure 4 and Table S1, Supporting Information. The right cluster of data points was calculated from simulations with 3456 molecules, whereas the left cluster of data points was calculated from simulations with 13 824 molecules.

parameters for an example reactive trajectory (250 K, 100 bar, spherical interface), and the sixth column of Table S1, Supporting Information, lists the observed induction times for all 114 reactive trajectories obtained in this study.

Figure 4 gives an indication of the trend in observed induction times (multiplied by liquid volume to directly compare systems of different sizes) as X_{CH_4} varies. Consistent with experimental results,^{10,13} induction times decrease with increasing X_{CH_4} . The scatter in induction time is also decreased at higher values of X_{CH_4} , evident from Figure 4 even without plotting the nonreactive

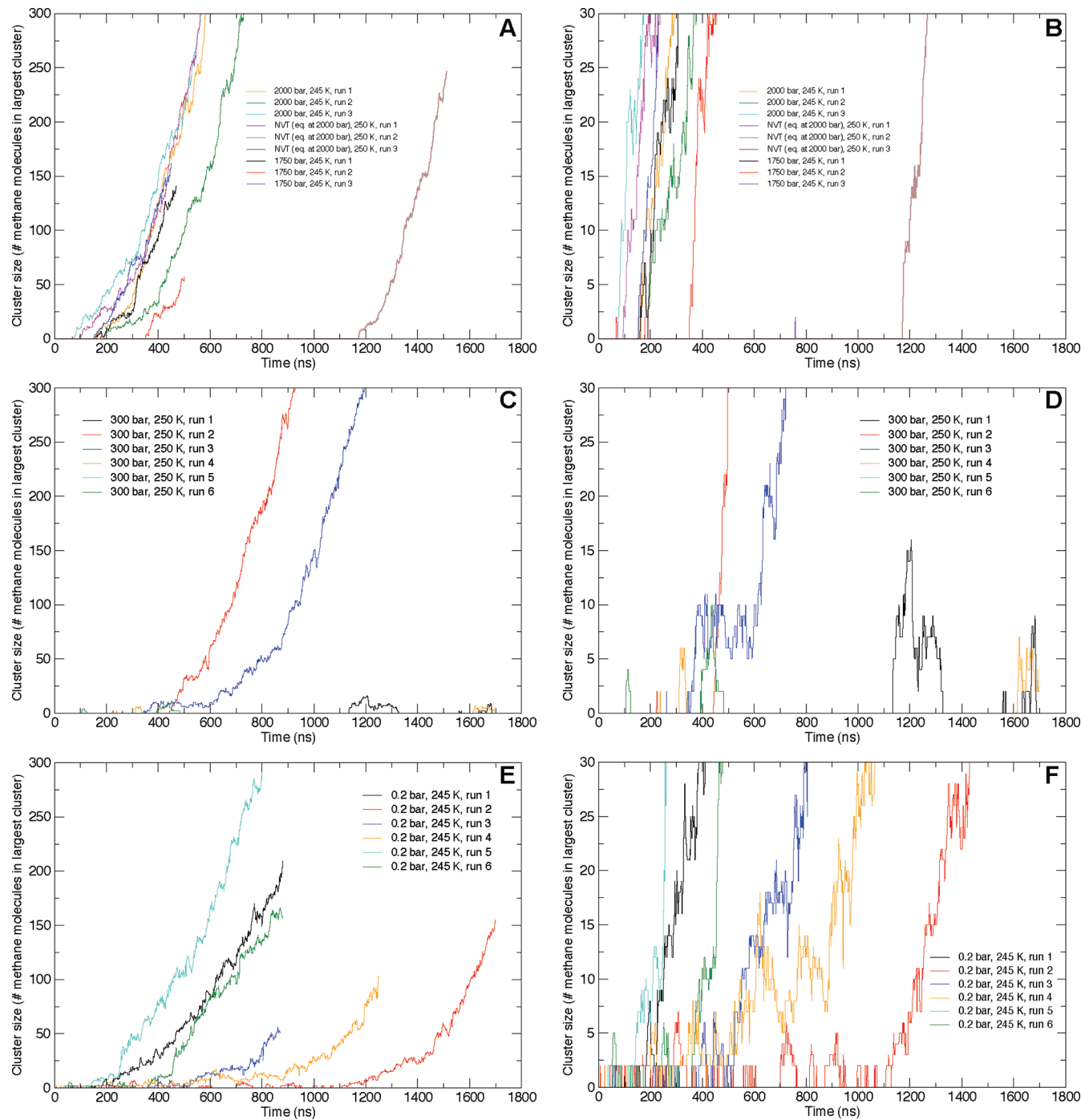


Figure 6. Evolution of the largest methane clusters in multiple simulations. Plots on the right show the same data as their counterparts on the left, but zoomed in by a factor of 10 on the ordinate. (A, B) Example simulations performed with 13 824 molecules (no interfacial curvature). (C, D) Example simulations performed with 3456 molecules (cylindrical interfacial curvature). (E, F) Example simulations performed with 3456 molecules (spherical interfacial curvature).

trajectories as lower bounds on induction times for the 59 non-reactive simulations. The spread in induction times apparent from Figure 4 and columns 3–6 of Table S1, Supporting Information, is consistent with the common assumption that nucleation is a stochastic process. However, the induction times observed in this work (in the extremely small simulated system volumes) are *at a maximum* on the order of several millionths of a second. Induction times of these magnitudes, when observed on

experimental time scales, would be considered immediate—that is, despite the obvious relative scatter in induction times and a clear separation of time scales (both of which distinguish nucleation from spinodal decomposition^{60–62}), we are likely operating in a regime beyond the *effective experimental spinodal* (which is an artifact of experimental time resolution).⁶³ Natarajan et al. refer to this effective spinodal boundary for the case of hydrate nucleation as X_{ml} , the dissolved guest concentration beyond which

nucleation occurs immediately;¹⁰ they postulate that this concentration limit is “greater than the maximum experimentally-observed gas composition in the liquid solution, and *far less than the gas composition in the hydrate phase.*” Our simulations indicate that this limit is indeed far less than the gas composition in the hydrate phase, consistent with their conjecture, though given our microsecond-scale induction times in nanometer-scale system sizes, the true value of X_{ml} (for typical experimental time resolutions) is likely even smaller than the range of aqueous methane mole fractions for which we observe nucleation (0.02–0.04). Nevertheless, our induction data clearly show stochasticity and a separation of time scales between the induction periods and the hydrate formation events, indicating a free-energy barrier to nucleation even at these highly subcooled conditions; this suggests areas for future study regarding the difference between the true thermodynamic spinodal (though the existence of a true spinodal for crystallization has not been proven⁶¹) and the effective experimental spinodal (nonetheless limited by the time resolution of experimental data acquisition) in complex, multicomponent first-order phase transitions such as hydrate nucleation.

3.3. Hydrate Nucleation Rates. Figure 5 shows the calculated hydrate nucleation rates for all the pressures, temperatures, and interfacial curvatures investigated, with prenucleation concentration plotted on the abscissa and nucleation rate plotted on the ordinate. The various symbols on the plot refer to sets of simulations performed at constant temperature and interfacial curvature at different pressures (pressure generally increasing from left to right within each data set). In general, there is a clear trend of increasing nucleation rate with increasing X_{CH_4} . Furthermore, the rates calculated in our smaller systems (those with curved interfaces) fall along the same monotonic increasing trend across a wide range of thermodynamic conditions (0.2–4000 bar, 245–275 K), consistent with experimental and theoretical studies citing guest concentration as a critical factor in the driving force for nucleation.^{10–13} An extreme example can be seen for the simulations at 245 K with spherical interfacial curvature. For simulations performed at barostat pressures as low as 0.2 bar, virtually all of the effective vapor phase pressure is caused by interfacial curvature. Nonetheless, the observed nucleation rates for these systems fall at the same point in the trend in Figure 5 as for systems with barostat pressures orders of magnitude higher than 0.2 bar, but with similar prenucleation concentrations.

The nucleation rates for our larger systems (with flat interfaces) fall noticeably higher than the trend shown in Figure 5 for our smaller simulation systems. In addition to the reduction in density fluctuations observed when simulating larger systems⁶⁴ combined with the decrease in nucleation probability in water systems with larger density fluctuations,⁶⁵ this difference in nucleation rate might be explained by a multiphase system size effect: interfacial solid destabilization. Consistent with MD simulations of ice nucleation,⁶⁶ the water phase in the immediate vicinity of the fluid–fluid interface remains disordered during our nucleation simulations, as shown in Movie S1, Supporting Information. Additionally, incipient hydrate nuclei that form near the interface (especially in the sliver of water between the periodic images of the nanobubbles in our smaller simulations) are observed to be susceptible to dissociation, shown in Movie S2, Supporting Information, and its accompanying plot of solid-like cluster evolution (Figure S3, Supporting Information). Due to the larger size of the flat-interface systems (and because the incipient hydrates often migrate several nanometers during nucleation), there is a higher probability in the larger systems

that the hydrates will grow without contacting the interface and dissociating, thus increasing the calculated nucleation rate compared with the smaller systems and explaining the offset between the two system sizes observed in Figure 5. This explanation is supported by Figure 6, showing the degree of solid-like clustering for multiple simulations of both system sizes. The plots in Figure 6 show that multiple unsuccessful nucleation attempts (e.g., Figure 6c,d, run 1) as well as delayed growth to postcritical behavior (e.g., Figure 6e,f, run 4) occur in the smaller systems, while such unsuccessful prenucleation attempts and growth delay are not observed in the larger systems (Figure 6a,b). Note also that the density of methane relative to its value in the bulk aqueous phase decreases by ~30% in the immediate vicinity of the methane–water interface, and this decrease begins between 0.5 and 1 nm from the interface; this observation is consistent with the reported depletion of solute (relative to its bulk concentration in the liquid) on the liquid side of a vapor–liquid interface in simulations of both N_2 and CO_2 vapor in contact with liquid water.⁶⁷ This phenomenon is shown for an example trajectory in Figure S4, Supporting Information, which also shows a local increase in water density as the interface is approached, beginning between 0.5 and 1 nm from the interface. These local density changes (especially the ~30% decrease in methane concentration) may help explain why the immediate vicinity of the interface is an unfavorable location for the formation of hydrates, and previous simulations of methane–water interfaces at hydrate forming conditions also suggest that the water near the interface is “more disordered”⁶⁸ compared with the bulk.

While a trend within the smaller system sizes between nucleation rate and aqueous methane concentration is clearly established in Figure 5, the above observations highlight the importance of considering system size effects when performing complex multiphase simulations. It is appropriate in this context to mention that an accurate definition of a critical nucleus to hydrate formation remains an outstanding challenge (especially a description of how the critical nuclei change with decreasing driving force). We stress that any multiphase MD investigation of hydrate critical nuclei be performed in systems large enough that *the effect of fluid–fluid interfacial dissociation is captured accurately and not overestimated via periodic boundary conditions* in small simulation systems.

4. CONCLUSIONS

We have shown that the expected trends in hydrate nucleation induction times and nucleation probability (within an arbitrary amount of simulation time) are observed with changes in pressure, temperature, and interfacial geometry and that the calculated hydrate nucleation rate increases with aqueous methane concentration across a range of thermodynamic conditions. Interfacial curvature can have a profound effect on X_{CH_4} and the observed nucleation rates and barostat settings necessary to yield spontaneous hydrate nucleation on currently accessible simulation time scales are at least an order of magnitude higher for simulations with flat methane–water interfaces compared with those with curved (spherical or cylindrical) interfaces at the same temperature. The surface of the liquid water phase remains disordered during nucleation, and the immediate vicinity of the methane–water interface is seen to have a destabilizing effect on incipient solids; this interfacial destabilization may explain why the calculated nucleation rates in our larger simulations fall higher than the trend observed in our smaller systems

when plotted against X_{CH_4} . The conditions studied here were necessarily highly metastable to hydrate formation in order to induce nucleation within a practical amount of computer time, and we anticipate that as parallel supercomputing power continues to increase, it will become possible to use the “brute force” technique employed here to achieve nucleation at smaller thermodynamic driving forces, approaching conditions more representative of experimental, geological, and industrial settings.

■ ASSOCIATED CONTENT

S Supporting Information. Figures S1–S4, Table S1, and Movies S1 and S2. This material is available free of charge via the Internet at <http://pubs.acs.org>.

■ AUTHOR INFORMATION

Corresponding Author

*E-mail address: asum@mines.edu.

■ ACKNOWLEDGMENT

This study was partially supported by the U.S. Department of Energy, Office of Basic Energy Sciences, Division of Materials Sciences and Engineering (DOE-BES award DE-FG02-05ER46242 for funding M.R.W. and partial support for C.A.K.) and the CSM Hydrate Consortium (presently sponsored by BP, Chevron, ConocoPhillips, ExxonMobil, Nalco, Petrobras, Shell, SPT Group, Statoil, and Total). A.K.S. and D.T.W. were partially supported by NSF Grant CBET-0933856. D.T.W. also acknowledges partial support from the Taiwan NSC during the preparation of this manuscript. The simulations were performed on facilities at the Golden Energy Computing Organization at the Colorado School of Mines using resources acquired with financial assistance from the NSF and the National Renewable Energy Laboratory. Computational time was partially provided by the National Renewable Energy Laboratory Computational Science Center, which is supported by the Office of Energy Efficiency and Renewable Energy of the United States Department of Energy under Contract DE-AC36-08GO28308. The authors thank Prof. Valeria Molinero for sharing with us a cage-recognition code and Da-Hye Park for updating that code to identify the main seven cage types observed in the nucleation simulations.

■ REFERENCES

- (1) Sloan, E. D.; Koh, C. A., *Clathrate Hydrates of Natural Gasses*; CRC Press: Boca Raton, FL, 2008.
- (2) Sloan, E. D. *Nature* **2003**, *426*, 353–363.
- (3) Johnson, J.; Torrice, M. *Chem. Eng. News* **2010**, *88*, 15–24.
- (4) Boswell, R. *Science* **2009**, *325*, 957–958.
- (5) Walsh, M. R.; Hancock, S. H.; Wilson, S. J.; Patil, S. L.; Moridis, G. J.; Boswell, R.; Collett, T. S.; Koh, C. A.; Sloan, E. D. *Energy Econ.* **2009**, *31*, 815–823.
- (6) Vorotyntsev, V. M.; Malyshev, V. M.; Mochalov, G. M.; Taraburo, P. G. *Theor. Found. Chem. Eng.* **2001**, *35*, 119–123.
- (7) Ogawa, T.; Ito, T.; Watanabe, K.; Tahara, K.-i.; Hiraoka, R.; Ochiai, J.-i.; Ohmura, R.; Mori, Y. H. *Appl. Therm. Eng.* **2006**, *26*, 2157–2167.
- (8) Mao, W. L.; Mao, H.-k.; Goncharov, A. F.; Guo, V. V. S. Q.; Hu, J.; Shu, J.; Hemley, R. J.; Somayazulu, M.; Zhao, Y. *Science* **2002**, *27*, 2247–2249.
- (9) Florusse, L. J.; Peters, C. J.; Schoonman, J.; Hester, K. C.; Dec, C. A. K. S. F.; Marsh, K. N.; Sloan, E. D. *Science* **2004**, *305*, 469–471.
- (10) Natarajan, V.; Bishnoi, P. R.; Kalogerakis, N. *Chem. Eng. Sci.* **1994**, *49*, 2075–2087.
- (11) Kashchiev, D.; Firoozabadi, A. *J. Cryst. Growth* **2002**, *243*, 476–489.
- (12) Kashchiev, D.; Firoozabadi, A. *J. Cryst. Growth* **2002**, *241*, 220–230.
- (13) Kashchiev, D.; Firoozabadi, A. *J. Cryst. Growth* **2003**, *250*, 499–515.
- (14) Ohmura, R.; Ogawa, M.; Yasuoka, K.; Mori, Y. H. *J. Phys. Chem. B* **2003**, *107*, 5289–5293.
- (15) Wilson, P. W.; Lester, D.; Haymet, A. D. J. *Chem. Eng. Sci.* **2005**, *60*, 2937–2941.
- (16) Jensen, L.; Thomsen, K.; Solms, N. v. *Chem. Eng. Sci.* **2008**, *63*, 3069–3080.
- (17) Davies, S. R.; Hester, K. C.; Lachance, J. W.; Koh, C. A.; Sloan, E. D. *Chem. Eng. Sci.* **2009**, *64*, 370–375.
- (18) Pietrass, T.; Gaede, H. C.; Bifone, A.; Pines, A.; Ripmeester, J. A. *J. Am. Chem. Soc.* **1995**, *117*, 7520–7525.
- (19) Koh, C. A.; Savidge, J. L.; Tang, C. C. *J. Phys. Chem.* **1996**, *100*, 6412–6414.
- (20) Subramanian, S.; Sloan, E. D. *Fluid Phase Equilib.* **1999**, *158–160*, 813–820.
- (21) Koh, C. A.; Wisbey, R. P.; Wu, X.; Westacott, R. E.; Soper, A. K. *J. Chem. Phys.* **2000**, *113*, 6390–6397.
- (22) Henning, R. W.; Schultz, A. J.; Thieu, V.; Halpern, Y. *J. Phys. Chem. A* **2000**, *104*, 5066–5071.
- (23) Moudrakovski, I. L.; Sanchez, A. A.; Ratcliffe, C. I.; Ripmeester, J. A. *J. Phys. Chem. B* **2001**, *105*, 12338–12347.
- (24) Staykova, D. K.; Kuhs, W. F.; Salamatina, A. N.; Hansen, T. *J. Phys. Chem. B* **2003**, *107*, 10299–10311.
- (25) Klapproth, A.; Goreshnik, E.; Staykova, D.; Klein, H.; Kuhs, W. F. *Can. J. Phys.* **2003**, *81*, 503–518.
- (26) Uchida, T.; Takeya, S.; Wilson, L. D.; Tulk, C. A.; Ripmeester, J. A.; Nagao, J.; Ebinuma, T.; Narita, H. *Can. J. Phys.* **2003**, *81*, 351–357.
- (27) Kini, R. A.; Dec, S. F.; Sloan, E. D. *J. Phys. Chem. A* **2004**, *108*, 9550–9556.
- (28) Schicks, J. M.; Ripmeester, J. A. *Angew. Chem., Int. Ed.* **2004**, *43*, 3310–3313.
- (29) Murshed, M. M.; Kuhs, W. F. *J. Phys. Chem. B* **2009**, *113*, 5172–5180.
- (30) Dec, S. F. *J. Phys. Chem. C* **2009**, *113*, 12355–12361.
- (31) Ohno, H.; Strobel, T. A.; Dec, S. F.; E. Dendy Sloan, J.; Koh, C. A. *J. Phys. Chem. A* **2009**, *113*, 1711–1716.
- (32) Baez, L. A.; Clancy, P. *Ann. N.Y. Acad. Sci.* **1994**, *715*, 177.
- (33) Radhakrishnan, R.; Trout, B. L. *J. Chem. Phys.* **2002**, *117*, 1786–1796.
- (34) Moon, C.; Taylor, P. C.; Rodger, P. M. *J. Am. Chem. Soc.* **2003**, *125*, 4706–4707.
- (35) Moon, C.; Hawtin, R. W.; Rodger, P. M. *Faraday Discuss.* **2007**, *136*, 367–382.
- (36) Hawtin, R. W.; Quigley, D.; Rodger, P. M. *Phys. Chem. Chem. Phys.* **2008**, *10*, 4853–4864.
- (37) Zhang, J.; Hawtin, R. W.; Yang, Y.; Nakagava, E.; Rivero, M.; Choi, S. K.; Rodger, P. M. *J. Phys. Chem. B* **2008**, *112*, 10608–10618.
- (38) Guo, G. J.; Li, M.; Zhang, Y. G.; Wu, C. H. *Phys. Chem. Chem. Phys.* **2009**, *11*, 10427–10437.
- (39) Walsh, M. R.; Koh, C. A.; Sloan, E. D.; Sum, A. K.; Wu, D. T. *Science* **2009**, *326*, 1095–1098.
- (40) Jacobson, L. C.; Hujo, W.; Molinero, V. *J. Am. Chem. Soc.* **2010**, *132*, 84112–80850.
- (41) Jacobson, L. C.; Hujo, W.; Molinero, V. *J. Phys. Chem. B* **2010**, *114*, 13796–13807.
- (42) Vatamanu, J.; Kusalik, P. G. *Phys. Chem. Chem. Phys.* **2010**, *12*, 15065–15072.
- (43) Jacobson, L. C.; Molinero, V. *J. Am. Chem. Soc.* **2011**, *133*, 6458–6463.
- (44) Bai, D.; Chen, G.; Zhang, X.; Wang, W. *Langmuir* **2011**, *27*, 5961–5967.

- (45) Guo, G.-J.; Zhang, Y.-G.; Liu, C.-J.; Li, K.-H. *Phys. Chem. Chem. Phys.* **2011**, *13*, 12048–12057.
- (46) Tamhane, A. C.; Dunlop, D. D. *Statistics and Data Analysis: From Elementary to Intermediate*; Prentice Hall: Upper Saddle River, NJ, 2000.
- (47) Attard, P.; Moody, M. P.; Tyrrell, J. W. G. *Phys. A* **2002**, *314*, 696–705.
- (48) Hess, B.; Kutzner, C.; van der Spoel, D.; Lindahl, E. *J. Chem. Theor. Comput.* **2008**, *4*, 435–447.
- (49) Jensen, L.; Thomsen, K.; von Solms, N.; Wierzchowski, S.; Walsh, M. R.; Koh, C. A.; Sloan, E. D.; Wu, D. T.; Sum, A. K. *J. Phys. Chem. B* **2010**, *114*, 5775–5782.
- (50) Conde, M. M.; Vega, C. *J. Chem. Phys.* **2010**, *113*, No. 064507.
- (51) Parrinello, M.; Rahman, A. *J. Appl. Phys.* **1981**, *52*, 7182–7190.
- (52) Hoover, W. G. *Phys. Rev. A* **1985**, *31*.
- (53) Abascal, J. L. F.; Sanz, E.; Fernández, R. G.; Vega, C. *J. Chem. Phys.* **2005**, *122*, No. 234511.
- (54) Goodbody, S. J.; Watanabe, K.; MacGowan, D.; Walton, J. P.; Quirke, N. *J. Chem. Soc. Faraday Trans.* **1991**, *87*, 1951–1958.
- (55) Miyamoto, S.; Kollman, P. A. *J. Comput. Chem.* **1992**, *13*, 952–962.
- (56) Essmann, U.; Perera, L.; Berkowitz, M. L.; Darden, T.; Lee, H.; Pedersen, L. G. *J. Chem. Phys.* **1995**, *103* (8577), 1–17.
- (57) Matsumoto, M.; Tanaka, K. *Fluid Dyn. Res.* **2008**, *40*, 546–553.
- (58) Jacobson, L. C.; Molinero, V. *J. Phys. Chem. B* **2010**, *114*, 7302–7311.
- (59) Walsh, M. R.; Rainey, J. D.; Lafond, P. G.; Park, D.-H.; T., G.; Beckham; Jones, M. D.; Lee, K.-H.; Koh, C. A.; Sloan, E. D.; Wu, D. T.; Sum, A. K. *Phys. Chem. Chem. Phys.* **2011**, DOI: 10.1039/C1CP21899A.
- (60) Chandler, D. *J. Chem. Phys.* **1978**, *68*, 2959–2970.
- (61) Trudu, F.; Donadio, D.; Parrinello, M. *Phys. Rev. Lett.* **2006**, *97*, No. 105701.
- (62) Wedekind, J.; Chkonia, G.; Wölk, J.; Strey, R.; Reguera, D. *J. Chem. Phys.* **2009**, *131*, 114506.
- (63) Langer, J. S. Kinetics of Metastable States. In *Systems Far from Equilibrium*; Sitges: Barcelona, 1980.
- (64) Allen, M. P.; Tildesley, D. J. *Computer Simulation of Liquids*; Oxford University Press: Oxford, 1987.
- (65) Matsumoto, M.; Saito, S.; Ohmine, I. *Nature* **2002**, *416*, 409–413.
- (66) Vrbka, L.; Jungwirth, P. *J. Phys. Chem. B* **2006**, *110*, 18126–18129.
- (67) Somasundaram, T.; in het Panhuis, M.; Lynden-Bell, R. M.; Patterson, C. H. *J. Chem. Phys.* **1999**, *111*, 2190–2199.
- (68) Reed, S. K.; Westacott, R. E. *Phys. Chem. Chem. Phys.* **2008**, *10*, 4614–4622.